

Geodesic distances in probabilistic spaces for patch-based ultrasound image processing

Cid A. N. Santos, *Student Member, IEEE*, and Nelson D. A. Mascarenhas, *Senior Member, IEEE*

Abstract—Many recent ultrasound image processing methods are based on patch comparison, such as filtering and segmentation. Identifying similar patches in noise corrupted images is a key factor for the performance of these methods. While the Euclidean distance is ideal to handle the patch comparison under additive Gaussian noise, finding good measures to compare patches corrupted by multiplicative noise is still an open research. In this study, we deduce several new geodesic distances, arising from parametric probabilistic spaces, and suggest them as similarity measures to process RF and log-compressed ultrasound images in patch-based methods. We provide practical examples using these measures in the fields of ultrasound image filtering and segmentation, with results that confirm the potential of the technique.

Index Terms—ultrasound imaging; geodesic distances; Rayleigh noise; Fisher-Tippett noise

I. INTRODUCTION

ULTRASONOGRAPHY is an important modality of medical imaging since it is non-invasive, harmless, portable, low-cost and allows the visualization of several structures of the human body. However, ultrasound (US) images are corrupted by speckle, a physical phenomenon that difficult the interpretation by physicists and hinder the performance of US patch-based image processing techniques. Currently, many of these techniques rely on the non-local paradigm introduced by the work in [1] and are known as patch-based methods. A central point in these patch-based methods is a measure of distance, or similarity, between patches. Originally proposed as the Euclidean distance for processing additive white Gaussian (AWG) noise, this measure is not adequate to handle the multiplicative nature of the speckle.

Some alternatives to the Euclidean distance have been used in patch-based methods dealing with the speckle noise in synthetic aperture radar (SAR) and US images, as seen in [2], [3], [4], [5], [6], [7], [8] and [9].

In [2], a Bayesian approach to the non-local means (NLM) algorithm [1] is used to filter US images. Instead of using the Euclidean distance, as in the original proposal, the Pearson distance is used as the measure of similarity between patches. The same Pearson distance is also used to replace the Euclidean distance in [3] to filter SAR images and in [10] to segment US images.

C. A. N. Santos is with the Computing Department, Federal University of São Carlos, São Carlos, Brazil and SIDIA R&D Institute, Manaus, Brazil.

N. D. A. Mascarenhas is with the Computing Department, Federal University of São Carlos, São Carlos, Brazil and Centro Universitário Campo Limpo Paulista, Campo Limpo Paulista, Brazil

The second author has a scholarship from CNPq, Brazil (Process 306742/2017-9).

The work in [4] uses the weighted maximum likelihood estimation framework [11] to derive a statistical measure of similarity between patches. This measure is used in a variant of the NLM algorithm to filter SAR images where the speckle is modeled as following a Rayleigh-Nakagami distribution.

In [5], stochastic distances based on the (h, ϕ) -divergence class are derived for the Wishart distribution and used as patch similarity measures in a variant of the NLM algorithm. This approach is used to filter SAR images. Also using stochastic distances based on the (h, ϕ) -divergence class, in [6], the distances are proposed for the Fisher-Tippett distribution and applied in a variant of the block-matching 3D (BM3D) [12] approach for filtering log-compressed US images.

Recent research is using geodesic distances based on probabilistic spaces to process speckle in SAR imagery. In [7] the geodesic distances between two G_0 distributions are used for region discrimination. Working with polarimetric SAR images, in [8], the geodesic distances are used to obtain the difference image in a change detection approach.

Based on the latest trend of image processing using convolutional neural networks (CNN), [9] uses a CNN with a strategy of residual learning for SAR image despeckling. The method is named SAR-CNN. The residual learning approach estimates the noise component and subtracts it from the noisy image. SAR-CNN is an adaptation of the work in [13], designed for Gaussian noise, where the Euclidean distance is replaced by a similarity measure derived from the statistics of the speckle and generated through the generalized likelihood ratio test, as proposed by the work in [14].

Contributions: In this article, we deduce several distance measures between US image patches that were modeled as being corrupted by Rayleigh and Fisher-Tippett noise. These measures represent the geodesic distances in the related probabilistic spaces and are based on well-known entropy measures. The geodesic distances derived here may be used to enhance the performance of US image processing techniques based on patch comparison. These measures are different from those recently proposed for SAR since they are based on different statistical models and entropy measures. These measures are also different from the geodesic distances based on the pixel intensity domain, which are commonly used in image segmentation, since they are based on different theories. Finally, while in this manuscript we explore the geodesic distances arising from statistical spaces, the work in [6] uses symmetrized versions of statistical divergences as similarity measures.

This article is organized as follows. In Section II we discuss some speckle statistical models for US image and explain the basic theory for deriving geodesic distances on

probabilistic spaces. We also introduce some filtering and segmentation methods to be used in the experimental section, including common quality metrics. Section III presents our main contribution, where we derive a set of similarity measures based on the noise models and previously discussed theory. In Section IV we provide examples on how the derived similarity measures can be used in patch-based US image processing methods. Finally, in Sections V and VI we present the experimental results and the conclusions.

II. TECHNICAL BACKGROUND

A. Ultrasound image statistics

The US image is acquired by transmitting high-frequency sound waves into the body and collecting the returning echoes. Scattering is the main physical phenomenon responsible for the returning echoes, which occurs due to the acoustic impedance mismatch between different media and due to the point source scattering particles.

The sum of the echoes which relate to a small body volume, the resolution cell, determines the ultrasonic radio frequency (RF) signal for that specific position. The amplitude of this signal depends on the acoustic properties (reflectivity) of the related resolution cell, and the speckle. The speckle is formed from the interferences by constructive and destructive echoes, giving the image a random granular pattern with particular statistical characteristics.

Two main factors are considered to model the speckle statistics, the placement (regular or random) and the density of scatterers. The various combinations of these factors yield different scattering regimes and, consequently, different statistical models for the speckle in the RF US signal.

Considering a resolution cell with a high density of scatterers (≥ 10), randomly distributed and without strong specular reflections, we have the regime referred as the fully developed speckle. In this case, the amplitude of the RF US signal envelope is known to be well described by a Rayleigh random variable (Y):

$$P(Y|\sigma) = \frac{Y}{\sigma^2} \exp\left(-\frac{Y^2}{2\sigma^2}\right), \quad Y \geq 0, \quad \sigma > 0. \quad (1)$$

where Y is the amplitude of the RF signal. The parameter σ of the Rayleigh distribution represents the tissue reflectivity for the specific resolution cell.

Regarding the RF US image, each pixel represents a resolution cell, and the tissue reflectivity (σ) associated with this resolution cell may be considered to be the gray level value of that pixel in the noiseless image.

If we have a patch of a RF US image represented by the samples $\{y_1, y_2, \dots, y_n\}$, the maximum likelihood estimator (MLE) of the σ parameter of the Rayleigh distribution is given by:

$$\hat{\sigma} = \sqrt{\frac{1}{2n} \sum_{i=1}^n y_i^2}. \quad (2)$$

Defining a new random variable by applying the logarithm transform to equation (1), we can model the log-compression

phase, which is carried out by any commercial US equipment, to adjust the large dynamic range of the RF image to the dynamic range of the equipment display:

$$Z = \log(Y + 1). \quad (3)$$

Notice that the Rayleigh random variable Y has support interval $[0, +\infty)$. By adding one in equation (3), we conveniently keep the new Z random variable in the same support interval since there should be no negative amplitudes in the log-transformed image.

The distribution of the transformed random variable Z will be given by:

$$P(Z) = \left| \frac{dY}{dZ} \right| P(Y). \quad (4)$$

From equation (3), we have

$$Y = \exp(Z) - 1. \quad (5)$$

and

$$\frac{dY}{dZ} = \exp(Z). \quad (6)$$

Replacing equation (5) in (1) and coupling its result with (6) in equation (4), we have the distribution for the log-compressed US image, modeled by Z in equation (3). This distribution has a double exponential or Fisher-Tippett shape, of which the only parameter is tissue reflectivity σ :

$$P(z|\sigma) = \left(\frac{\exp(z) - 1}{\sigma^2} \right) \exp\left(z - \frac{(\exp(z) - 1)^2}{2\sigma^2}\right). \quad (7)$$

Considering $\{z_1, z_2, \dots, z_n\}$ as samples of independent and identically distributed observations from the distribution of Z in equation (7), the joint density function for all observations (likelihood function) is given by:

$$\begin{aligned} L &= P(y_1, y_2, \dots, y_n|\sigma) \\ &= \prod_{i=1}^n \left[\left(\frac{\exp(z_i) - 1}{\sigma^2} \right) \exp\left(z_i - \frac{(\exp(z_i) - 1)^2}{2\sigma^2}\right) \right]. \end{aligned} \quad (8)$$

Applying the log to transform the product in a sum, we have the log-likelihood function:

$$\begin{aligned} \log(L) &= \sum_{i=1}^n \log(\exp(z_i) - 1) - \sum_{i=1}^n \log(\sigma^2) \\ &\quad + \sum_{i=1}^n z_i - \sum_{i=1}^n \left(\frac{(\exp(z_i) - 1)^2}{2\sigma^2} \right). \end{aligned} \quad (9)$$

By taking the derivative of the log-likelihood, with respect to σ , and making it equal to zero, we find the maximum likelihood estimator for the parameter σ of the Fisher-Tippett distribution defined in equation (7):

$$\hat{\sigma} = \sqrt{\frac{1}{2n} \sum_{i=1}^n (\exp(z_i) - 1)^2}. \quad (10)$$

B. Multiplicative model

Assuming a fully developed speckle model and, consequently, Rayleigh statistics for the speckle, if we consider a homogeneous region of the image (σ constant), the ratio of the standard deviation to the expected value is constant, which means that they are proportional:

$$\frac{\sqrt{\frac{4-\pi}{2}}\sigma}{\sqrt{\frac{\pi}{2}}\sigma} = \sqrt{\frac{4-\pi}{\pi}} \approx 0.5227. \quad (11)$$

The fact that the standard deviation is proportional to the mean in homogeneous areas suggests a multiplicative model for the speckle. Such model is widely used for deriving speckle reducing schemes, being expressed as:

$$I(i, j) = S(i, j)Y(i, j). \quad (12)$$

where $Y(i, j)$ is the multiplicative speckle noise in the spatial position (i, j) , with statistics given by equation (1). Moreover, $S(i, j)$ represents the noiseless pixel value to be recovered for the same spatial position.

Applying a homomorphic approach is a form of addressing speckle under the multiplicative model. This is based on using the logarithm to transform the multiplicative noise into additive noise:

$$\begin{aligned} \log[I(i, j)] &= \log[S(i, j)] + \log[Y(i, j)], \\ \log[I(i, j)] &= \log[S(i, j)] + Z(i, j). \end{aligned} \quad (13)$$

where $Z(i, j)$ is now an additive log-transformed speckle noise.

Similarly to the work in [6], here we adopt the multiplicative model when dealing with RF US images, and the homomorphic approach when handling the log-compressed US images. When adopting these models, we must be aware that it assumes at least two main simplifications. First, a fully developed speckle model is valid mainly in homogeneous areas, not in the whole US image. Second, usually, the logarithm transform phase of a commercial US equipment will not be as simple as the model shown in equation (3) and may involve other non-linear operations that change the speckle statistics.

C. Geodesic distances based on probabilistic spaces

Considering $f_P(x; \theta)$ as a parametric family of probability distributions, where $\theta = \{\theta_1, \theta_2, \dots, \theta_M\}$ is a M-dimensional parameter vector, the set of all possible values of this parameter vector form a M-dimensional Riemannian space, as shown by Rao in [15]. Also in [15], Rao studied the geometric structure of this space, introducing a quadratic differential metric that allows the geodesic distance between two points in this space to be calculated. In summary, the geodesic distance proposed by Rao is a measure of distance between two parameterizations from a family of probability distributions

Additionally, the studies [16] and [17] introduced a generic method to calculate Rao's geodesic distance based on the ϕ -entropy class. In [18] this previous method is extended and considers the (h, ϕ) -entropy class. Entropy classes are generalizations that allow the representation of a set of entropies. The (h, ϕ) -entropy class can be expressed as

$$H_{(h, \phi)}(s) = h \left(\sum_i \phi(p_i) \right), \quad (14)$$

where choosing adequate functions h and ϕ result in well known entropy measures. Table I shows a set of entropies and the related h and ϕ functions used to obtain them based on the (h, ϕ) -entropy class.

The method proposed by the study in [18] allows the calculation of generalizations of Rao's geodesic distance, based on all entropy measures that can be represented by the (h, ϕ) -entropy class. Considering a family of distributions with only one parameter, this method can be summarized as: consider P a random variable with density $f_P(x; \theta)$ and support interval I , where $\theta = \{\theta_1\}$ is the parameter vector. The geodesic distance between the points θ_a and θ_b in the space generated by the parameter vector of the density $f_P(x; \theta)$, expressed in terms of the (h, ϕ) -entropy class, is given by [18]:

$$d(\theta_a, \theta_b) = \left| \int_{\theta_a}^{\theta_b} [g(\theta)]^{\frac{1}{2}} d\theta \right|, \quad (15)$$

where

$$\begin{aligned} g(\theta) &= \left[h'' \left[\int_I \phi(f_P(x; \theta)) dx \right] \right. \\ &\quad \left. 2 \int_I \phi'(f_P(x; \theta)) \frac{\partial f_P(x; \theta)}{\partial \theta} dx \right. \\ &\quad \left. + \left[h' \left[\int_I \Phi(f_P(x; \theta)) dx \right] \right. \right. \\ &\quad \left. \left. \int_I \phi''(f_P(x; \theta)) \frac{\partial f_P(x; \theta)^2}{\partial \theta^2} dx \right] \right], \end{aligned}$$

assuming that the integrals exist and are finite. The symbols h'/ϕ' and h''/ϕ'' denote the first and second derivatives of the functions $h(y)$ and $\phi(x)$ with respect to y and x respectively.

The formulation presented here is only for densities with unidimensional parameter vectors. We did this for simplicity, since the formulation for multidimensional parameter vectors is far more complex and will not be used in this study.

D. Image filtering quality metrics

This section provides references on some objective image quality metrics that will be used in the experimental section to quantify the performance of the despeckling filters. The following convention will be considered for the description of the metrics within the next topics: I_f represents the filtered image, I_g represents the ground truth noiseless image, M and N are the image dimensions, (i, j) refers to the spatial position of a pixel. Note that the metrics requiring I_g , known as full-reference metrics, cannot be applied to real US images since the ground truth is not available.

1) *Speckle smoothing metrics (SSI/MPSSI)*: In a homogeneous region of a RF US image, the speckle strength, or speckle index (SI), is given by the relation between the standard deviation and the mean. As defined in [19], the speckle suppression index (SSI) is obtained from normalizing the speckle index of the filtered image by the speckle index of the original image. Notice that after log-compression, the

TABLE I
ENTROPIES- (h, ϕ) AND RESPECTIVE $h(x)$ AND $\phi(x)$ FUNCTIONS.

(h, ϕ) -Entropy	$h(y)$	$\phi(x)$
Arimoto	$\frac{(y^s - 1)}{s - 1}$	$x^{\frac{1}{s}}, s > 0, s \neq 1$
Havrda-Charvát	y	$\frac{(x^s - x)}{1 - s}, s > 0, s \neq 1$
Rényi	$\frac{\log(y)}{(s-1)}, s > 0, s \neq 1$	x^s
Shannon	y	$-x \log(x)$
Sharma e Mittal	$\frac{\exp[(s-1)y] - 1}{1 - s}, s > 0, s \neq 1$	$x \log(x)$
Tsallis	$\frac{y-1}{1-s}, s > 0, s \geq 1$	x^s
Varma	$\frac{\log(y)}{m-r}, m - 1 < r < m, m \geq 1$	x^{r-m+1}

mean is no longer proportional to the standard deviation, thus, the SSI must be calculated using the variance, as in [20, p.37]. When the filter suppresses speckle, $SSI < 1$, and the lower the SSI is, the stronger suppression abilities the filter has.

The SSI is not reliable when the filter overestimates the filtered image mean. To avoid this, the mean preservation speckle suppression index (MPSSI) is defined in [21]. Lower MPSSI values indicate better filter performance preserving the mean while removing the speckle[21].

The SSI and $MPSSI$ are calculated for each individual pixel of the image, in a 7×7 window centered on the pixel. The global SSI and $MPSSI$ associated with the image is the mean value of the pixels. Additionally, SSI and $MPSSI$ should be calculated only for homogeneous regions of the image. To decide if a pixel belongs to a homogeneous area, we use the result of [22], where the speckle index (named coefficient of variation) is used as an edge detector. The authors show that the local SI is approximately equal to the global SI for the homogeneous areas of an RF image. The local SI (SI_{local}) refers to the SI calculated in a patch of the image, and the global (SI_{global}) refers to the SI calculated for the whole image. For this study, we determined experimentally that pixels with $SI_{local} \leq 0.9 * SI_{global}$ belong to homogeneous areas.

2) *Peak signal-to-noise ratio (PSNR)*: Peak signal-to-noise ratio is the ratio between the maximum power of a signal and the power of the disturbing noise and it can be expressed as [23]:

$$PSNR = 10 \log_{10} \frac{L^2}{MSE} \quad (16)$$

where L is the maximum possible pixel value (power) of the image, typically 255 for a gray level, 8 bits coded image. The mean squared error (MSE) represents the noise power and it can be expressed as [23]:

$$MSE = \frac{1}{MN} \sum_{i,j=1}^{M,N} (I_g(i,j) - I_f(i,j))^2 \quad (17)$$

The higher the PSNR, the higher the relation between the signal and noise, consequently, the better the filtering process.

3) *Edge preservation index (EPI)*: We used the metric defined by the study in [24] as the measure for the edge preservation capabilities of the filters:

$$EPI = \frac{\sum_{i,j=1}^{M,N} D_g(i,j) * D_f(i,j)}{\left(\sum_{i,j=1}^{M,N} D_g(i,j)^2\right) \left(\sum_{i,j=1}^{M,N} D_f(i,j)^2\right)} \quad (18)$$

where $D_g = (\Delta I_g - E[\Delta I_g])$, $D_f = (\Delta I_f - E[\Delta I_f])$ and Δ represents the high-pass filtered version of the image, obtained with a 3×3 pixel standard approximation of the Laplacian operator.

The edge preservation index ranges in the interval $[0, 1]$, and values near 1 indicate better filter performance in preserving the edges.

4) *Resolution index(RI)*: The metric adopted to measure the resolution of the US image in this study is the same found in [25] [26] [27]. We named it resolution index. The index is computed as the percentage of pixels in the auto-correlation function of the filtered image that exceeds 75% of its maximum value. Lower RI values usually indicate better image resolution.

E. Image segmentation performance metrics

This section provides references on some metrics to quantify the performance of the segmentation method.

The output of a segmentation process consists in partitioning the dataset having all the image pixels. The ground truth image provides the perfect partitioning for the same dataset. Thus, several measures can be defined by comparing these two partition sets.

1) *Jaccard index (JI)*: Jaccard index is used to measure the similarity between two sets, defined as the ratio of the intersection of the two sets divided by their union [28]. The index ranges from 0 to 1 and the higher the index, the higher the similarity between sets.

2) *Rand index (RAND)*: The Rand index is a measure of the accuracy of the segmentation, as defined in [29]. The index ranges in the interval $[0, 1]$, in which the value 0 indicates that the ground truth and segmented image are completely different, and the value 1 indicates that they are equal.

3) *Global consistency error (GCE)*: The global consistency error is a measure of the error in the segmentation, as defined in [30]. The scale ranges from 0 to 1 and the lower the value, the better the segmentation.

4) *Variation of information (VI)*: The variation of information is a measure of distance typically used to compare two partitions of the same dataset, as defined in [31].

III. GEODESIC DISTANCES DERIVATION

In this section we apply the theory exposed in section II-C to derive the geodesic distance on the probabilistic spaces defined by the Rayleigh and Fisher-Tippett distributions, and based on the (h, ϕ) -entropies shown in Table I.

A. Geodesic distances for Rayleigh distribution

Consider P_1 and P_2 as two noisy patches that can be statistically described by the Rayleigh distribution given by equation (1), and with parameter vectors $\theta_1 = \{\sigma_1\}$ and $\theta_2 = \{\sigma_2\}$, respectively.

Replacing equation (1) in equation (15), using a pair of $h(y)$ and $\phi(x)$ functions given in Table I, and solving the integrals in the interval $[0, +\infty]$, we can deduce the following geodesic distances:

a) Arimoto geodesic distance for Rayleigh distribution:

$$d_{ari}^{ray}(\sigma_1, \sigma_2) = \frac{2^{\frac{7-s}{4}} s^{\frac{s+1}{4}}}{\Gamma\left(\frac{s+1}{2}\right)^{-s/2}} \left| \frac{\left(\sigma_2^{\frac{s-1}{2}} - \sigma_1^{\frac{s-1}{2}}\right)}{(s-1)(s+1)^{\frac{-1}{2}}} \right|, \quad (19)$$

where $s > 0$ and $s \neq 1$. The symbol Γ denotes the gamma function, as defined in [32, p.255].

b) Havrda-Charvát geodesic distance for Rayleigh distribution:

$$d_{hc}^{ray}(\sigma_1, \sigma_2) = \left| \frac{2^{\frac{s+3}{4}} \left(\sigma_1^{\frac{1-s}{2}} - \sigma_2^{\frac{1-s}{2}}\right) s^{\frac{-s-3}{4}}}{(s-1)((s^2+3)\Gamma\left(\frac{s+1}{2}\right))^{\frac{-1}{2}}} \right|, \quad (20)$$

where $s > 0$ and $s \neq 1$.

c) Rényi geodesic distance for Rayleigh distribution:

$$d_{re}^{ray}(\sigma_1, \sigma_2) = \left| \sqrt{\frac{s+3}{s}} \log\left(\frac{\sigma_2}{\sigma_1}\right) \right|, \quad (21)$$

where $s > 0$.

d) Shannon geodesic distance for Rayleigh distribution:

$$d_{hc}^{ray}(\sigma_1, \sigma_2) = 2 \left| \log\left(\frac{\sigma_2}{\sigma_1}\right) \right|. \quad (22)$$

e) Sharma-Mittal geodesic distance for Rayleigh distribution:

$$d_{sm}^{ray}(\sigma_1, \sigma_2) = \left| \frac{\left(\sigma_1^{\frac{1-s}{2}} - \sigma_2^{\frac{1-s}{2}}\right) (s+3)^{\frac{1}{2}}}{2^{-\frac{s+3}{4}} \exp\left(\frac{2+\gamma}{(4s-4)^{-1}}\right) (s-1)} \right|, \quad (23)$$

where $s > 0$ and $s \neq 1$. The symbol γ denotes the Euler-gamma constant, as defined in [32, p.255].

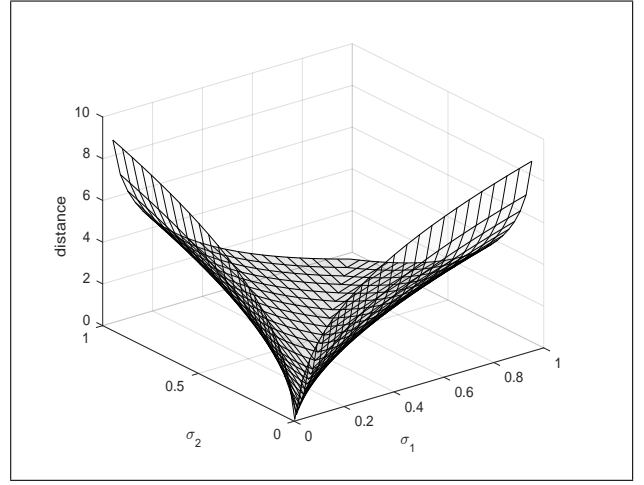


Fig. 1. Variation of the Havrda-Charvát geodesic distance for two Rayleigh distributions of parameters σ_1 and σ_2 , when $s = 0.5$.

f) Tsallis geodesic distance for Rayleigh distribution:

$$d_{ts}^{ray}(\sigma_1, \sigma_2) = \left| \frac{2^{\frac{s+3}{4}} \left(\sigma_1^{\frac{1-s}{2}} - \sigma_2^{\frac{1-s}{2}}\right) s^{\frac{-s-3}{4}}}{(s-1)((s^2+3)\Gamma\left(\frac{s+1}{2}\right))^{\frac{-1}{2}}} \right|, \quad (24)$$

where $s > 0$ and $s \neq 1$.

g) Varma geodesic distance for Rayleigh distribution:

$$d_{var}^{ray}(\sigma_1, \sigma_2) = \left| \sqrt{1 + \frac{3}{1-m+r}} \log\left(\frac{\sigma_2}{\sigma_1}\right) \right|, \quad (25)$$

where $m-1 < r < m$ and $m \geq 1$.

These geodesic distances depend only on the reflectivity parameters σ_1 and σ_2 that can be estimated from the noisy patches using the MLE given by equation (2). Figure 1 shows a graph that serves as an example of how the Havrda-Charvát geodesic distance varies with σ_1 and σ_2 , when $s = 0.5$. Observing the graph, we note that the geodesic distance is always evaluated to zero when $(\sigma_1 = \sigma_2)$.

From our research and literature reviews, the geodesic distances associated with the Arimoto, Havrda-Charvát, Rényi, Shannon, Sharma-Mittal, Tsallis and Varma entropies had not yet been derived for the Rayleigh distribution.

B. Geodesic distances for the Fisher-Tippett distribution

Consider P_1 and P_2 as two noisy patches that can be statistically described by the Fisher-Tippett distribution given by equation (7), and with parameter vectors $\theta_1 = \{\sigma_1\}$ and $\theta_2 = \{\sigma_2\}$, respectively.

Replacing equation (7) in equation (15), using a pair of $h(y)$ and $\phi(x)$ functions given in Table I, and solving the integrals in the interval $[0, +\infty]$, we can deduce the following geodesic distances:

a) Arimoto geodesic distance for Fisher-Tippett:

$$d_{ari}^{ft}(\sigma_1, \sigma_2) = 2^{\frac{3-s}{2}} \Gamma\left(\frac{1}{s}\right)^{s/2} \left| \sqrt{s} \log\left(\frac{\sigma_2}{\sigma_1}\right) \right|, \quad (26)$$

where $s > 0$.

b) *Havrda-Charvát geodesic distance for Fisher-Tippett:*

$$d_{hc}^{ft}(\sigma_1, \sigma_2) = 2^{\frac{s+1}{2}} s^{-\frac{s}{2}} \left| \sqrt{\Gamma(s)} \log \left(\frac{\sigma_2}{\sigma_1} \right) \right|, \quad (27)$$

where $s > 0$.

c) *Rényi para geodesic distance for Fisher-Tippett:*

$$d_{re}^{ft}(\sigma_1, \sigma_2) = 2 \left| \log \left(\frac{\sigma_2}{\sigma_1} \right) \right|. \quad (28)$$

d) *Shannon geodesic distance for Fisher-Tippett:*

$$d_{re}^{ft}(\sigma_1, \sigma_2) = 2 \left| \log \left(\frac{\sigma_2}{\sigma_1} \right) \right|. \quad (29)$$

e) *Sharma-Mittal geodesic distance for Fisher-Tippett:*

$$d_{re}^{ft}(\sigma_1, \sigma_2) = 2e^{\frac{1}{2}(-\gamma-1+\log(2))(s-1)} \left| \log \left(\frac{\sigma_2}{\sigma_1} \right) \right|, \quad (30)$$

where $s > 0$.

f) *Tsallis geodesic distance for Fisher-Tippett:*

$$d_{re}^{ft}(\sigma_1, \sigma_2) = \sqrt{2^{s+1} s^{-s}} \sqrt{|\Gamma(s)|} \left| \log \left(\frac{\sigma_2}{\sigma_1} \right) \right|, \quad (31)$$

where $s > 0$.

g) *Varma geodesic distance for Fisher-Tippett:*

$$d_{var}^{ft}(\sigma_1, \sigma_2) = 2 \left| \log \left(\frac{\sigma_2}{\sigma_1} \right) \right|. \quad (32)$$

These geodesic distances depend only on the reflectivity parameters σ_1 and σ_2 that can be estimated from the noisy patches using the MLE given by equation (10). Figure 2 shows a graph that serves as an example of the derived measures and how the Havrda-Charvát geodesic distance varies with σ_1 and σ_2 , when $s = 0.5$. Observing the graph, we note that the geodesic distance is always evaluated to zero when $(\sigma_1 = \sigma_2)$.

From our research and literature reviews, the geodesic distances associated with Arimoto, Havrda-Charvát, Rényi, Shannon, Sharma-Mittal, Tsallis and Varma entropies had not yet been derived for the Fisher-Tippett distribution.

The computational complexity of calculating the geodesic distances corresponds to the computational complexity of calculating the MLE of the patches, which is linear, according to equation (10) for the Fisher-Tippett distribution. This analysis is also valid for the geodesic distances derived in Section III-A for the Rayleigh distribution, according to its MLE in equation (2).

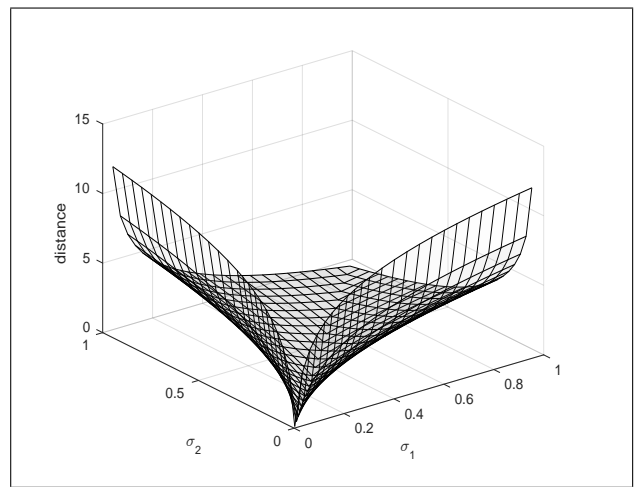


Fig. 2. Variation of the Havrda-Charvát geodesic distance for the Fisher-Tippett distribution of parameters σ_1 and σ_2 , when $s = 0.5$.

IV. EXPERIMENTS

To show practical examples on how the geodesic distances derived in this study can be used to process US images, we designed experiments applying these distances to filtering and segmentation approaches that are based on patch comparison. We note that the following experiments were designed solely to demonstrate that the derived distances can improve the performance of patch-based methods when processing US images. A study to compare a specific method using these distances to other methods found in the literature is yet to be performed.

A. test images

We used synthetic and real US images, both in RF and log-compressed formats, for the experiments using filtering and segmentation. The procedures to prepare these images are described below.

1) *synthetic images:* The experiments with synthetic images use the database of realistic breast phantoms found in [33]. The phantoms mimic the breast tissue echogenicities, tumor shapes, and lesion histology. There are three types of lesions (carcinoma, cyst, and fibroadenoma), with three possible tumor shapes each. For each combination of lesion/tumor shape, there are 50 phantoms, where the position of the tumor varies. We used 10 phantoms from each combination, totaling 90 tested phantoms. These phantoms are the ground truth or noiseless images. Next, we define a noise pattern as an image with Rayleigh-distributed amplitudes of mean 1 and the same size of the ground truth. Since we consider uncorrelated noise, the noisy image must be obtained by the pixel-by-pixel multiplication of the noiseless image and the noise pattern. These noisy images are referred to as synthetic RF noisy images. We note that this noisy image corresponds to the US multiplicative noise model in equation (12), where the speckle noise corresponds to the Rayleigh distribution in equation (1). The synthetic log-compressed images are obtained by log-compressing the synthetic RF noisy images using equation (3). We also note that the log-compressed image is related to the

US homomorphic noise model in equation (13), where the speckle is represented by the Fisher-Tippett distribution in equation (7). After all procedures, we use a central part of the images sized 256×256 pixels.

2) *real images*: The experiments with real images use a set of RF frames of breast lesion recorded from a malignant and a benign tumor, available from [34]. The sets are composed by 183 RF frames for each type of tumor. We used 50 RF frames from each set for our experiments. These images are in RF format, thus we extracted the envelope of the signal using the Hilbert transform, as suggested in [35]. These are the images referred to as the real RF US images. The real log-compressed images are obtained by log-compressing the real RF images, as the model in equation (3). After all procedures, we use a central part of the images sized 256×256 pixels.

B. Filtering

1) *Filtering with NLM*: For the first experiment we used a pixel-wise non-local means approach, as described in [36]. In that implementation, designed for Gaussian noise, the image is divided in overlapping windows, named research windows, with a central pixel p . The estimation of the pixel p in the filtered image is a weighted mean using all the pixels q_i within the research window, where the weight is based on an exponential kernel depending on the squared Euclidean distance between the patches:

$$w_i = \exp\left(-\frac{d(B(p, f), B(q_i, f))^2}{h^2}\right). \quad (33)$$

where $B(x, f)$ denotes a patch centered in the pixel x and size $(2f + 1) \times (2f + 1)$. The parameter h controls the degree of smoothness the filter will apply on the image.

To define a version based on geodesic distances, we replaced the Euclidean distance in equation (33) by one of the geodesic distances deduced for Rayleigh distribution in Section III-A. This procedure is similar to the approach found in [5], however, we used geodesic distances.

Next, we applied the original NLM using the Euclidean distance and the geodesic distance NLM variant to filter RF US images. Tables II and III show the performance of the filters applied to RF synthetic and real US images respectively. The performance is measured according to the metrics found in Section II-D. The tables present the mean values for the entire dataset. Figure 3 presents sample images of the filtering result when using synthetic images.

We note that in Tables II and III the value for the RI metric is the same for all filters. By fixing one of the metrics we can compare the filters based on the other metrics. To fix the RI metric we ran one of the filters first to measure it, then we ran the other filters and varied their parameters until the same RI was obtained.

2) *Filtering with BM3D*: Our second filtering experiment used the BM3D algorithm, which is one of the state of the art algorithms for filtering AWG noise corrupted images. The BM3D algorithm performs three core operations: block-matching, 3D collaborative filtering in a sparse domain, and reconstruction. For the block-matching operation, the image is

TABLE II
METRIC RESULTS WHEN FILTERING SYNTHETIC RF US IMAGES USING RAYLEIGH GEODESIC AND EUCLIDEAN DISTANCES AS MEASURES OF SIMILARITY IN NLM (BEST RESULTS IN BOLDFACE).

Distance	PSNR	EPI	SSI	MPSSI	RI
Arimoto	16.212	0.324	0.562	0.693	0.019
Havrda-Charvát	16.225	0.331	0.542	0.694	0.019
Rényi	16.199	0.321	0.570	0.692	0.019
Shannon	16.208	0.321	0.570	0.692	0.019
Sharma-Mittal	16.221	0.330	0.542	0.694	0.019
Tsallis	16.225	0.331	0.542	0.694	0.019
Varma	16.199	0.321	0.570	0.692	0.019
Euclidean	16.182	0.252	0.648	1.527	0.019

TABLE III
METRIC RESULTS WHEN FILTERING REAL RF US IMAGES USING RAYLEIGH GEODESIC AND EUCLIDEAN DISTANCES AS MEASURES OF SIMILARITY IN NLM (BEST RESULTS IN BOLDFACE).

Distance	SSI	MPSSI	RI
Arimoto	0.411	2.836	14.882
Havrda-Charvát	0.440	2.438	14.882
Rényi	0.445	2.439	14.882
Shannon	0.445	2.439	14.882
Sharma-Mittal	0.440	2.438	14.882
Tsallis	0.440	2.438	14.882
Varma	0.445	2.439	14.882
Euclidean	0.440	4.913	14.882

scanned in overlapping windows, and for each of these windows, a reference patch is compared to all other (overlapping) patches within the window. All similar patches, according to Euclidean distance, are stacked to form a 3D block. These 3D blocks undergo a linear transformation and are filtered in a sparse domain. After inverse transformation, there are many estimates for the same pixel, and the patch is reconstructed by combining those estimates. The *BM3D* algorithm executes the core operations twice. In the first step, the *3D* blocks are filtered using a sparse coefficient threshold; during the second step, the *3D* blocks are filtered using a Wiener filter with coefficients estimated from the result of the first step.

For our experiments, we used the implementation of the *BM3D* algorithm found in [37]. To implement a version of the *BM3D* based on geodesic distances, we replaced the Euclidean distance in the block-matching step by one of the geodesic distances deduced for the Fisher-Tippett distribution in Section III-B. This procedure is similar to the proposal found in [6], however, we used geodesic distances.

Next, we applied the original *BM3D* using the Euclidean distance and the geodesic distance *BM3D* variant to filter the log-compressed US images. Tables IV and V present the performance of the filters applied to synthetic log-compressed, and real log-compressed US images, respectively. The performance is measured according to the metrics found in Section II-D, and the RI metric was also fixed. The tables present the mean values for the entire dataset. Figure 4 presents sample images of the filtering result when using synthetic images log-compressed US images.

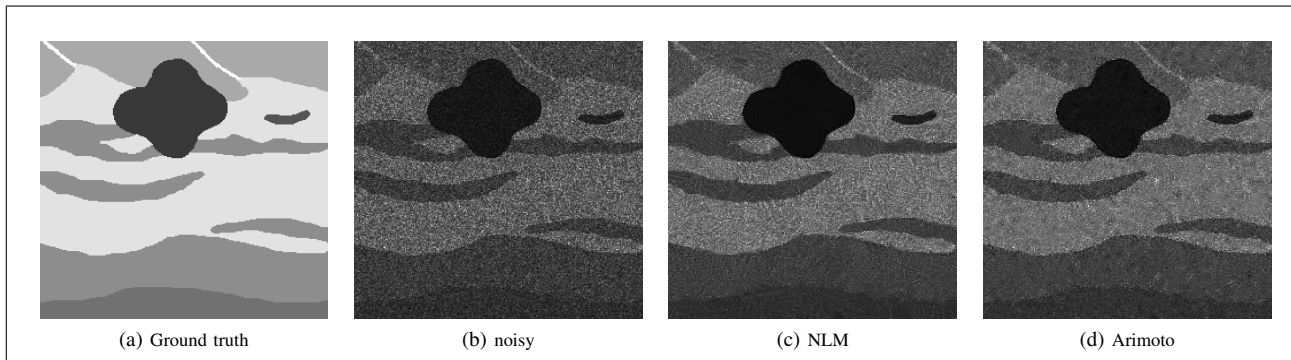


Fig. 3. Synthetic RF US image denoised by NLM and geodesic-based-NLM.

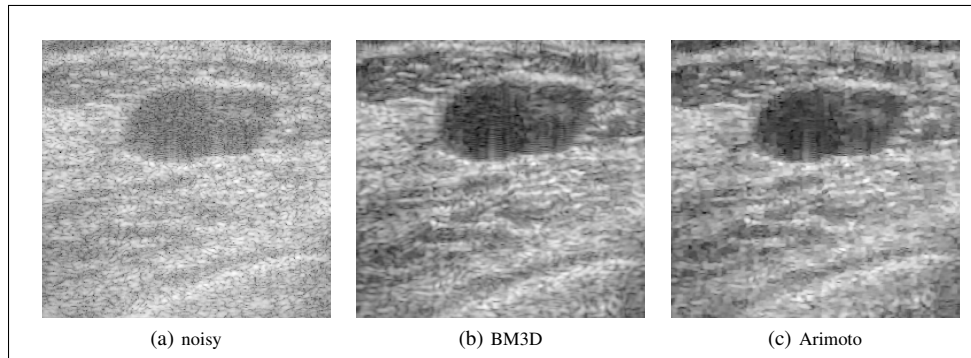


Fig. 4. Real log-compressed US image denoised by BM3D and geodesic-based-BM3D.

TABLE IV

METRIC RESULTS WHEN FILTERING SYNTHETIC LOG-COMPRESSED US IMAGES USING ORIGINAL BM3D AND GEODESIC-BASED-BM3D FOR THE FISHER-TIPPETT DISTRIBUTION (BEST RESULTS IN BOLDFACE).

Distance	PSNR	EPI	SSI	MPSSI	RI
Arimoto	29.394	0.517	0.042	0.065	0.028
Havrda-Charvát	29.394	0.517	0.042	0.065	0.028
Rényi	29.394	0.517	0.042	0.065	0.028
Shannon	29.394	0.517	0.042	0.065	0.028
Sharma-Mittal	29.394	0.517	0.042	0.065	0.028
Tsallis	29.394	0.517	0.042	0.065	0.028
Varma	29.394	0.517	0.042	0.065	0.028
Euclidean	29.113	0.382	0.058	0.101	0.028

TABLE V

METRIC RESULTS WHEN FILTERING REAL LOG-COMPRESSED US IMAGES USING ORIGINAL BM3D AND GEODESIC-BASED-BM3D FOR THE FISHER-TIPPETT DISTRIBUTION (BEST RESULTS IN BOLDFACE).

Distance	SSI	MPSSI	RI
Arimoto	0.222	0.164	1.079
Havrda-Charvát	0.222	0.164	1.079
Rényi	0.222	0.164	1.079
Shannon	0.222	0.164	1.079
Sharma-Mittal	0.222	0.164	1.079
Tsallis	0.222	0.164	1.079
Varma	0.222	0.164	1.079
Euclidean	0.237	0.187	1.079

C. Segmentation

To compare the geodesic distances defined in Sections III-A and III-B with the Euclidean distance in an image segmentation algorithm, we used the US segmentation approach proposed in [10]. In this method, the image is represented

by a graph where the nodes are the pixels and the weight of the edge between two nodes x_i and x_j is defined as:

$$w(x_i, x_j) = \begin{cases} \exp\left(-\frac{d(F(x_i), F(x_j))}{h^2}\right) & , \text{for } x_j \in N_a(x_i). \\ 0, & \text{otherwise.} \end{cases} \quad (34)$$

where $d(F(x_i), F(x_j))$ is a similarity measure between the image descriptors located at pixels (nodes) x_i and x_j , and $N_a(x)$ is a neighborhood window centered at x and of size $a \times a$ pixels. The parameter h is a scaling factor of the weight matrix. After building the graph, a semi-supervised min-cut approach is applied for image segmentation. The approach is semi-supervised because it is necessary to manually provide the internal and external limits of the tumor shape using connected lines or ellipses.

Two types of descriptors are used as patch similarity measures. First, as in the original article, $d(F(x_i), F(x_j))$ is the Euclidean distance between the patches centered at x_i and x_j , and calculated in the neighborhoods $N_a(x_i)$ and $N_a(x_j)$. Second, we defined two variants based on geodesic distances, one for Rayleigh distribution and the other for the Fisher-Tippett distribution. For the Rayleigh distribution, $d(F(x_i), F(x_j))$ is one of the geodesic distances derived in Section III-A, calculated for the patches centered at x_i and x_j , and using the neighborhoods $N_a(x_i)$ and $N_a(x_j)$. Similarly, the variant for the Fisher-Tippett distribution uses the geodesic distances derived in Section III-B.

We used the same database of breast phantoms found in [33] for these experiments. The phantoms mimic the breast echogenicities and contain tumor shapes that can be easily

TABLE VI
PERFORMANCE OF THE SEGMENTATION WHEN USING THE RAYLEIGH-BASED AND THE EUCLIDEAN DISTANCE DESCRIPTORS (BEST RESULTS IN BOLDFACE).

Distance	Jl	RI	GCE	VI
Rayleigh-Arimoto	0.876	0.982	0.016	0.121
Rayleigh-Havrda-Charvát	0.865	0.980	0.017	0.130
Rayleigh-Rényi	0.875	0.981	0.016	0.122
Rayleigh-Shannon	0.878	0.982	0.016	0.119
Rayleigh-Shama-Mittal	0.877	0.982	0.016	0.121
Rayleigh-Tsallis	0.870	0.981	0.017	0.127
Rayleigh-Varma	0.850	0.977	0.019	0.142
Euclidean	0.728	0.950	0.036	0.247

TABLE VII
PERFORMANCE OF THE SEGMENTATION WHEN USING THE FISHER-TIPPETT-BASED AND THE EUCLIDEAN DISTANCE DESCRIPTORS (BEST RESULTS IN BOLDFACE).

Distance	Jl	RI	GCE	VI
Fisher-Tippett-Arimoto	0.873	0.981	0.016	0.123
Fisher-Tippett-Havrda-Charvát	0.870	0.980	0.016	0.125
Fisher-Tippett-Rényi	0.870	0.981	0.017	0.125
Fisher-Tippett-Shannon	0.870	0.981	0.017	0.125
Fisher-Tippett-Sharma-Mittal	0.867	0.980	0.017	0.127
Fisher-Tippett-Tsallis	0.871	0.981	0.016	0.124
Fisher-Tippett-Varma	0.870	0.981	0.017	0.125
Euclidean	0.737	0.952	0.035	0.240

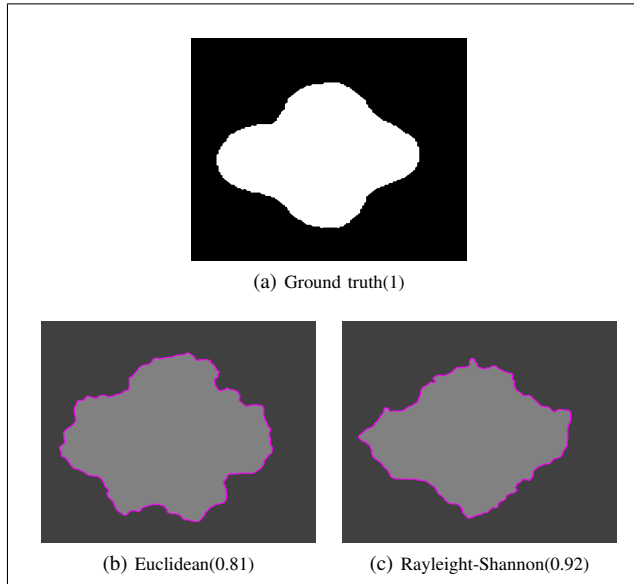


Fig. 5. Ground truth and segmented images using Euclidean, and Rayleigh-Shannon descriptors with related Jaccard index.

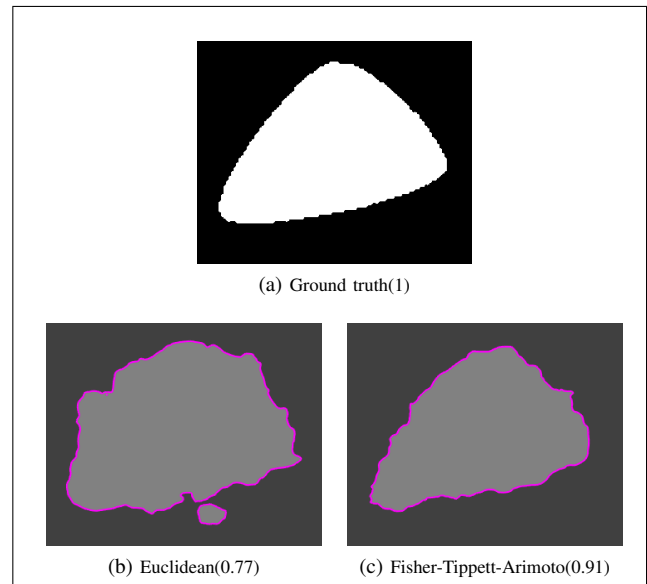


Fig. 6. Ground truth and segmented images using Euclidean and Fisher-Tippett-Arimoto descriptors with related Jaccard index.

separated from the image to serve as the segmentation ground truth. The database contains nine possible combinations of lesions/tumor shapes. We used one sample from each and repeated the tests 10 times, for 90 tests total.

Table VI presents the performance of the segmentation when using Rayleigh-based and Euclidean distance descriptors to segment the RF US images, measured by the metrics defined in Section II-E. Figure 5 shows the segmentation for one of the images.

Table VII presents the performance of the segmentation when used Fisher-Tippett-based and Euclidean distance descriptors to segment the log-compressed US images, measured by the metrics defined in Section II-E. Figure 6 shows the segmentation for one of the images.

V. DISCUSSION

The previous section presented practical examples of the usage of the similarity measures defined in Section III. We performed experiments using NLM and BM3D patch-based denoising algorithms and a patch-based segmentation approach.

The results in Tables III and II show that the NLM algorithm performed better when denoising both synthetic and RF US

images with the use of geodesic distances derived in this research as a replacement for Euclidean distance. For the synthetic images, the geodesic distances based on the Havrda-Charvát and Tsallis entropies presented slightly better results than the distances derived from the other entropies.

When using the BM3D algorithm with synthetic and real log-compressed US images, Tables IV and V also show that the denoising performance is better when using the geodesic distances derived in Section III. We note that on these tables there are no metric differences when comparing the different geodesic distances. This occurs because the distances are used to select the 16 or 32 patches more similar to the reference patch in the block-matching phase of the BM3D variant, thus there will be few differences in the patch set when using different geodesic distances.

Finally, Tables VI and VII show that replacing the Euclidean distance with geodesic distances improves the performance of the segmentation approach in all quality metrics. This is valid for the geodesic distances based on all the entropies and is valid for both RF and log-compressed synthetic US images.

The performance improvement when using geodesic distances seems to be in accordance with theoretical considerations since those measures are more adapted to the statistics of

the speckle noise than the Euclidean distance is. Consequently, we can suppose that not only the approaches shown in the experimental section will benefit from the use of geodesic distances, but possibly will benefit also all those methods using a measure of similarity to process US image patches that currently rely on the Euclidean distance.

We have used here only the traditional filtering and segmentation methods. In any case, the geodesic distances may also be used with the recent deep learning methods, if they need a similarity measure to compare patches, as in [9].

VI. CONCLUSIONS AND FUTURE RESEARCH

This study presented a set of geodesic distances based on the probabilistic spaces given by Rayleigh and Fisher-Tippett distributions. Those distances replace Euclidean distances to be used as measures of similarity in modified versions of patch-based filtering and segmentation approaches. Our experiments were performed on real and synthetic US images, both in RF and log-compressed formats. Good results in our tests suggest that the derived measures can improve patch-based methods that need to compare patches when processing US images.

The measures presented in this research are only valid for RF and log-compressed US images, modeled as fitting a Rayleigh or Fisher-Tippett distributions, respectively. For future research, similar measures can be derived for other statistical models as Nakagami and Log-Nakagami distributions.

A research comparing the geodesic distances derived in this study to other forms of similarity measures between patches contaminated by speckle noise is also necessary. Examples of distances to be compared could be the stochastic distances used in [5] and [6], or the Pearson distance used in [2]. We note that for doing this comparison, it would be necessary to adapt all the measures for the same statistical model.

REFERENCES

- [1] A. Buades, B. Coll, and J. M. Morel, "A review of image denoising algorithms, with a new one," *SIAM Journal on Multiscale Modeling and Simulation*, vol. 2, pp. 490–530, 2005.
- [2] P. Coupé, P. Hellier, C. Kervrann, and C. Barillot, "Nonlocal means-based speckle filtering for ultrasound images," *IEEE Trans. Image Process.*, vol. 18, no. 10, pp. 2221–2229, 2009. [Online]. Available: <http://dx.doi.org/10.1109/TIP.2009.2024064>
- [3] S. Parrilli, M. Poderico, C. V. Angelino, and L. Verdoliva, "A nonlocal SAR image denoising algorithm based on LLMSE wavelet shrinkage," *IEEE Trans. Geoscience and Remote Sensing*, vol. 50, no. 2, pp. 606–616, 2010. [Online]. Available: <http://ieeexplore.ieee.org/document/5989862/>
- [4] C. A. Deledalle, L. Denis, and F. Tupin, "Iterative weighted maximum likelihood denoising with probabilistic patch-based weights," *IEEE Trans. Image Process.*, vol. 18, no. 12, pp. 2661–2672, 2009.
- [5] L. Torres, S. J. S. Sant'Anna, C. da Costa Freitas, and A. C. Frery, "Speckle reduction in polarimetric SAR imagery with stochastic distances and nonlocal means," *Pattern Recognition*, vol. 47, pp. 141–157, 2014.
- [6] C. A. N. Santos, D. L. N. Martins, and N. D. A. Mascarenhas, "Ultrasound image despeckling with stochastic distances based-BM3D," *IEEE Trans. Image Process.*, vol. 26, no. 6, pp. 2632–2643, 2017.
- [7] J. Naranjo-Torres, J. Gambini, and A. C. Frery, "The geodesic distance between G_T^0 models and its application to region discrimination," *IEEE Journal of Selected Topics in Applied Earth Observations and Remote Sensing*, vol. 10, no. 3, pp. 987–997, 2017.
- [8] D. Ratha, S. De, T. Celik, and A. Bhattacharya, "Change detection in polarimetric SAR images using a geodesic distance between scattering mechanisms," *IEEE Geoscience and Remote Sensing Letters*, vol. PP, no. 99, pp. 1–5, 2017.
- [9] G. Chierchia, D. Cozzolino, G. Poggi, and L. Verdoliva, "SAR image despeckling through convolutional neural networks," *IEEE International Geoscience and Remote Sensing Symposium (IGARSS)*, pp. 5438–5441, 2017.
- [10] A. Ciurte, X. Bresson, O. Cuisenaire, N. Houhou, S. Nedeveschi, J.-P. Thiran, and M. B. Cuadra, "Semi-supervised segmentation of ultrasound images based on patch representation and continuous min cut," *PLoS ONE*, vol. 9, no. 7, pp. 1–14, 2014. [Online]. Available: <http://doi.org/10.1371/journal.pone.0100972>
- [11] J. Polzehl and V. Spokoiny, "Propagation-separation approach for local likelihood estimation," *Probability Theory and Related Fields*, vol. 135, no. 3, pp. 335–362, 2006.
- [12] K. Dabov, A. Foi, V. Katkovnik, and K. O. Egiazarian, "Image denoising by sparse 3-D transform-domain collaborative filtering," *IEEE Trans. Image Process.*, vol. 16, no. 8, pp. 2080–2095, 2007. [Online]. Available: <http://dblp.uni-trier.de/db/journals/tip/tip16.html#DabovFKE07>
- [13] K. Zhang, W. Zuo, Y. Chen, D. Meng, and L. Zhang, "Beyond a gaussian denoiser: Residual learning of deep CNN for image denoising," *IEEE Transactions on Image Processing*, vol. 26, no. 7, pp. 3142–3155, July 2017.
- [14] C. A. Deledalle, L. Denis, and F. Tupin, "How to compare noisy patches? patch similarity beyond gaussian noise," *Int. Journal of Computer Vision*, vol. 99, no. 1, pp. 86–102, 2012. [Online]. Available: <https://hal-institut-mines-telecom.archives-ouvertes.fr/hal-00672357>
- [15] C. R. Rao, "Information and accuracy attainable in the estimation of statistical parameters," *Bull. Calcutta Math. Soc.*, vol. 37, no. 3, pp. 81–91, 1945.
- [16] J. Burbea and C. R. Rao, "Entropy differential metric, distance and divergence measures in probability spaces: A unified approach," *Journal of Multivariate Analysis*, vol. 12, pp. 575–596, 1982.
- [17] —, "On the convexity of some divergence measures based on entropy functions," *IEEE Transactions on Information Theory*, vol. 28, no. 3, pp. 489–495, 1982.
- [18] M. L. Menéndez, D. Morales, L. Pardo, and M. Salicrú, "(h, Φ)-entropy differential metric," *Applications of Mathematics*, vol. 42, no. 2, pp. 81–98, 1997. [Online]. Available: <http://dx.doi.org/10.1023/A:1022214326758>
- [19] A. Shamsoddini and J. C. Trinder, "Image texture preservation in speckle noise suppression," in *Int. Society for Photogrammetry and Remote Sensing TC VII Symp.*, Vienna, Austria, July 2010, pp. 239–244.
- [20] C. Loizou and C. Pattichis, *Despeckle Filtering for Ultrasound Imaging and Video, Volume II: Selected Applications, Second Edition*, ser. Synthesis digital library of engineering and computer science. Morgan & Claypool Publishers, 2015. [Online]. Available: <https://books.google.com.br/books?id=kk8AaswEACAAJ>
- [21] S. G. Dellepiane and E. Angiati, "Quality assessment of despeckled SAR images," *IEEE J. Sel. Topics Appl. Earth Observ. in Remote Sens.*, vol. 7, no. 2, pp. 691–707, 2014.
- [22] M. Mora, C. Tauber, and H. Batatia, "Robust level set for heart cavities detection in ultrasound images," in *Computers in Cardiology*. Lyon, France: IEEE, Sep. 2005, pp. 235–238.
- [23] Z. Wang and A. C. Bovik, "Mean Square Error : Love It or Leave It," *IEEE IEEE Signal Process. Mag.*, vol. 26, no. Jan., pp. 98–117, 2009. [Online]. Available: <http://ieeexplore.ieee.org/lpdocs/epic03/wrapper.htm?arnumber=4775883>
- [24] F. Sattar, L. Florey, G. Salomonsson, and B. Lövnström, "Image enhancement based on a nonlinear multiscale method," *IEEE Trans. Image Process.*, vol. 6, no. 6, pp. 888–895, 1997. [Online]. Available: <http://dx.doi.org/10.1109/83.585239>
- [25] T. Taxt, "Restoration of medical ultrasound images using two-dimensional homomorphic deconvolution," *IEEE IEEE Trans. Ultrason., Ferroelect., Freq. Control*, vol. 42, no. 4, pp. 543–554, 1995.
- [26] O. V. Michailovich and A. Tannenbaum, "Despeckling of medical ultrasound images," *IEEE IEEE Trans. Ultrason., Ferroelect., Freq. Control*, vol. 53, no. 1, pp. 64–78, 2006.
- [27] J. F. Al-Asad, A. M. Reza, and U. Techavipoo, "An ultrasound image despeckling approach based on principle component analysis," *Int. Journal of Image Processing*, vol. 8, no. 4, pp. 156–177, 2014.
- [28] H.-H. Chang, A. H. Zhuang, D. J. Valentino, and W.-C. Chu, "Performance measure characterization for evaluating neuroimage segmentation algorithms," *NeuroImage*, vol. 47, no. 1, pp. 122–135, 2009. [Online]. Available: <http://dblp.uni-trier.de/db/journals/neuroimage/neuroimage47.html#ChangZVC09>
- [29] W. Rand, "Objective criteria for the evaluation of clustering methods," *Journal of the American Statistical Association*, vol. 66, no. 336, pp. 846–850, 1971.

- [30] D. Martin, C. Fowlkes, D. Tal, and J. Malik, "A database of human segmented natural images and its application to evaluating segmentation algorithms and measuring ecological statistics," in *IEEE Int. Conf. Computer Vision*, vol. 2, July 2001, pp. 416–423.
- [31] M. Meila, "Comparing clusterings—an information based distance," *Journal of Multivariate Analysis*, vol. 98, no. 5, pp. 873–895, 2007.
- [32] M. Abramowitz and I. A. Stegun, *Handbook of Mathematical Functions with Formulas, Graphs, and Mathematical Tables*, 9th ed. New York: Dover, 1970.
- [33] W. G. Flores, W. C. A. Pereira, and A. F. C. Infantosi, "Breast ultrasound despeckling using anisotropic diffusion guided by texture descriptors," *Ultrasound in Medicine & Biology*, vol. 40, no. 11, pp. 2609–2621, 2014.
- [34] M. F. Insana. Rf ultrasound patient data. [Online]. Available: http://ultrasonics.bioengineering.illinois.edu/data_patient.asp
- [35] G. Georgiou and F. Cohen, "Statistical characterization of diffuse scattering in ultrasound images," *IEEE Trans. Ultrason. Ferroelect. Freq. Control*, vol. 45, no. 1, pp. 57–64, 1998.
- [36] A. Buades, B. Coll, and J. M. Morel, "Non-local means denoising," *Image Processing On Line*, vol. 1, pp. 208–212, 2011.
- [37] M. Lebrun, "An analysis and implementation of the bm3d image denoising method," *Image Processing On Line*, vol. 2, pp. 175–213, 2012.